PHOTONICS Research

Ultraviolet-to-microwave room-temperature photodetectors based on three-dimensional graphene foams

Yifan Li,[1] Yating Zhang,[1,*] Yu Yu,[1] Zhiliang Chen,[1] Qingyan Li,[1] Tengteng Li,[1] Jie Li,[1] Hongliang Zhao,[1] Quan Sheng,[1,4] Feng Yan,[2,5] Zhen Ge,[3] Yuxin Ren,[3] Yongsheng Chen,[3] and Jianquan Yao[1,6]

[1]Key Laboratory of Optoelectronics Information Technology (Tianjin University), Ministry of Education, School of Precision Instruments and Optoelectronics Engineering, Tianjin University, Tianjin 300072, China
[2]Department of Applied Physics and Materials, Research Centre, The Hong Kong Polytechnic University, Hong Kong, China
[3]National Institute for Advanced Materials, Tianjin Key Laboratory of Metal and Molecule Based Material Chemistry, Key Laboratory of Functional Polymer Materials, Collaborative Innovation Center of Chemical Science and Engineering (Tianjin), School of Materials Science and Engineering, Nankai University, Tianjin 300071, China
[4]e-mail: shengquan@tju.edu.cn
[5]e-mail: apafyan@polyu.edu.hk
[6]e-mail: jqyao@tju.edu.cn
*Corresponding author: yating@tju.edu.cn

Received 15 October 2019; revised 17 December 2019; accepted 25 December 2019; posted 3 January 2020 (Doc. ID 380249); published 27 February 2020

Highly sensitive broadband photodetection is of critical importance for many applications. However, it is a great challenge to realize broadband photodetection by using a single device. Here we report photodetectors (PDs) based on three-dimensional (3D) graphene foam (GF) photodiodes with asymmetric electrodes, which show an ultra-broadband photoresponse from ultraviolet to microwave for wavelengths ranging from 10^2 to 10^6 nm. Moreover, the devices exhibit a high photoresponsivity of 10^3 A $\cdot$ W^{-1}, short response time of 43 ms, and 3 dB bandwidth of 80 Hz. The high performance of the devices can be attributed to the photothermoelectric (PTE, also known as the Seebeck) effect in 3D GF photodiodes. The excellent optical, thermal, and electrical properties of 3D GFs offer a superior basis for the fabrication of PTE-based PDs. This work paves the way to realize ultra-broadband and high-sensitivity PDs operated at room temperature.

https://doi.org/10.1364/PRJ.380249

1. INTRODUCTION

Photodetectors (PDs) play an essential role in many photoelectronic systems such as biological and chemical sensors, imaging, optical communications, missile guidance, and remote sensing [1–8]. However, PDs with wide spectral response range, especially in the terahertz (THz) and microwave regions at room temperature, are difficult to realize because in the THz and microwave regions, photon energies are too low to excite the charge carriers across the bandgap in traditional semiconductors, such as Si [9–11]. As for narrow-bandgap semiconductors, the fast-quenching effect may influence the response in the THz and microwave regions, especially at elevated temperatures [10,12]. Therefore, it is challenging to realize a broad spectral band response through direct excitations across the bandgap.

The photothermoelectric (PTE) effect (also known as the Seebeck effect) may provide an opportunity to cover a wide response range through thermoelectric conversion, which is caused by a light-induced temperature gradient across different materials contained within a device [13–16]. Theoretically, PTE PDs can realize an ultra-broadband spectral response through some appropriate materials, from ultraviolet (UV) to microwave, because thermoelectric processing is insensitive to and independent of the wavelength. Various novel nanomaterials have been used in PTE PDs, including nanowires and two-dimensional (2D) materials [15,17–20]. As a typical representative 2D material, graphene shows extraordinary optical and electronic characteristics [21–23]. However, suffering from their inherent properties, which include small areas [15,16], complex structures, and low optical absorption (2.3% for a single layer) [24], single- or few-layer graphene PDs always present a low photoresponse in the UV to THz range at room temperature [25,26]. Therefore, highly sensitive PTE PDs have been rarely reported until now.

In this work, we prepare three-dimensional (3D) graphene foam (GF) diode PDs based on an asymmetric gold (Au)/3D GF/titanium (Ti) structure for the first time. The 3D GF, composed of multiple cross-linked graphene sheets, not only inherits the advantages of graphene but also presents a stronger absorption capacity, enhancement of thermal properties, and long-ranging conductive network [1,27–29]. Additionally, a large area and hyperelasticity are also accessible for GF owing to the significant advances in material synthesis [30]. The devices present ultra-broadband and highly efficient absorption spectra ranging from 300 nm to 1 mm. As a result of the high absorption, PTE effect, and long-ranging conductive network, the GF PDs exhibit an ultra-broadband, flat, and high photoresponsivity at a low bias voltage at room temperature.

2. DEVICE STRUCTURE AND FABRICATION

A. Synthesis of 3D GFs

The 3D GFs were synthesized by a solvothermal method. The graphene oxide (GO) ethanol solution (0.5 mg/mL) was thermally treated in a Teflon-lined autoclave at 180°C for 12 h to form an intermediate solid. After the solvent was exchanged from ethanol to water, the sponge was freeze-dried to remove the remaining water. Finally, the sample was annealed at 800°C for 2 h.

B. Fabrication Process of the Au/3D GF/Ti

The Au/3D GF/Ti photodetectors were fabricated as follows. A 3D GF sample with dimensions of 14 mm × 14 mm × 2 mm was prepared using a laser cutting machine. The as-prepared 3D GF samples were then transferred carefully on silica glass sheets and handled within a UV-ozone system for 15 min. After the transfer process was complete, the samples were placed in a vacuum chamber with a vacuum of 10^{-4} Pa. The electrodes were then prepared by the thermal evaporation method using shadow masks on the 3D GF, where one set was made from Cr/Au (10/200 nm) and the other was made from Cr/Ti (10/200 nm).

C. Characterization and Testing

The *I*–*V* characteristics and the photocurrents of the 3D GF were measured using a Keithley 2400 source meter with LabVIEW software. The light sources were 405, 532, 808, 1064, and 1170 nm semiconductor lasers; 9.6, 10, and 10.6 μm carbon dioxide (CO_2) gas lasers; a 118 μm terahertz source (FIRL 100); and 220 GHz radio-frequency signal. The light power was tested using a power meter with an RS232 port (Ophir Vega). The broadband response and the absorption spectra of the device were tested using a Zolix Omni-λ 3007 spectrophotometer with Si and InGaSn photodetectors. The absorption performance of the 3D GF was tested using a terahertz time-domain spectroscopy system. The infrared spectrum of the 3D GF was tested using a Fourier transform infrared (FTIR) spectrophotometer with potassium bromide (KBr) pellets. The temperature distribution image was recorded by the infrared thermal imager (FLIR T630sc). The 3D GF's surface morphology was examined using a scanning electron microscope. The Raman spectrum was obtained using a Renishaw laser Raman spectrometer.

3. RESULTS AND DISCUSSION

Figure 1(a) shows the architecture of a GF PD with a size of 14 mm × 14 mm. SiO_2 was used as a substrate, the active layer of the device was GF [31], and the channel size was determined to be 6 mm according to the distance between the two electrodes. To amplify the PTE current of the GF PD, two metal electrodes (i.e., Au and Ti) were designed and deposited by thermal evaporation. Figure 1(b) shows the scanning electron microscopy (SEM) image of GF with a scale bar of 100 μm and an amplified image with a scale bar of 10 μm. Three-dimensionally cross-linked graphene sheets with 3D porous architecture were assembled to form a 3D structure in the micro- and nanometer scales [31,32]. To confirm the degree of reduction, a contrast Raman measurement of graphene oxide (GO) and the GF was performed. As shown in Fig. 1(c), D and G peaks were present at 1350 cm^{-1} and 1580 cm^{-1}, respectively, for both GO and 3D GF. Significantly, the intensity ratio of the D to G peaks for GF increased to 1.28 from 0.93 obtained for GO. This demonstrated a large decrease in the defect number and the formation of graphene layers after the reduction reaction [33,34].

As a further characterization, the absorption spectra of 3D GF are shown in Figs. 1(d)–1(f). There is no instrument that can cover such a wide spectral range from UV to microwave. Thus, we used three instruments to measure three successive wavelength regions. The first optical spectrum was obtained by a grating monochromator and tungsten. The 3D GF exhibited a flat and broadband absorption within the range from 400 to 2200 nm and showed an obvious superiority over GO in the entire range, owing to the porous structure [35]. The insets show the photographs of a 3D GF pillar with a diameter of 15 mm and a height of 30 mm. All samples used in this work were cut from this 3D GF pillar.

The second part of the absorption spectrum was obtained using an FTIR spectrophotometer, typically ranging from 4000 to 400 cm^{-1}. To provide consistency and clarity, we used the wavelength as the horizontal axis (2.5–25 μm) and absorption as the vertical axis, as shown in Fig. 1(e). The absorption

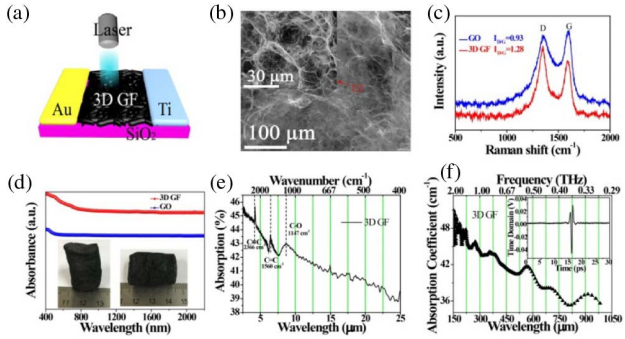

Fig. 1. (a) Schematic structure of the 3D GF photodetector. (b) SEM image of the 3D GF with the magnification scales of 100 μm and 10 μm. (c) Raman spectra of 3D GF (red line) and GO (blue line). (d) Absorption spectra of 3D GF (red line) and GO (blue line) over the range from 400 to 2200 nm. The inset pictures exhibit the 3D GF columnar. (e) FTIR spectrum of 3D GF ranging from 2.5 to 25 μm. (f) The THz-TDS spectrum of 3D GF ranging from 150 to 1000 μm.

consistently decreased over the whole region, except for the peaks at 1147, 1560, and 2366 cm^{-1}, which corresponded to the symmetric and antisymmetric stretching vibrations of C—O, C═O, and C≡O groups in GF, respectively.

The third region was obtained from terahertz time-domain (THz-TDS) spectroscopy with a range from 0.2 to 2 THz. For the compatibility consideration, we again used the wavelength as the abscissa (150–1000 μm) and absorption coefficient as the ordinate as depicted in Fig. 1(f). The inset shows the original signal in the time domain. After the frequency transformation, the absorption from 150 to 1000 μm was acquired. The absorption for all the samples decreased gradually over the THz region with minor differences. Consistent with the previous reports, the 3D GF showed an ultra-broadband and flat downtrend in absorption characteristics over a wide range from the UV to THz region [36,37].

Next, we will present the photoelectric characteristics of GF PDs. The current–voltage (*I–V*) characteristics under varying irradiances of a laser are given in Fig. 2(a). Here we used a 532 nm laser as a typical representative. In the dark, the *I–V* curve was at a low level and increased with the gradual increase of illumination. Good contact between the 3D GF and two electrodes was attributed to an ohmic contact, which is very conducive to the PTE photocurrent.

There are several vital parameters that are generally used to assess the photoresponse performance of a detector, which include the photoresponsivity (R), the detectivity (D^*), the noise equivalent power (NEP), and the response time [38]. The photoresponsivity, which describes the photoelectric conversion capability of a device, is given by [38]

$$R = \frac{\Delta I}{P} = \frac{I_{\text{illu}} - I_{\text{dark}}}{E_e \times A}, \tag{1}$$

where ΔI is the photocurrent defined as $I_{\text{illu}} - I_{\text{dark}}$, as I_{illu} and I_{dark} are the current with and without illumination,

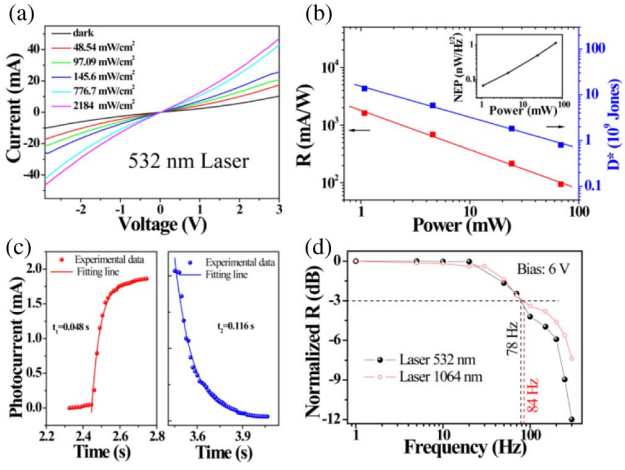

Fig. 2. (a) Current–voltage (*I–V*) characteristics in the dark and with different illumination intensities of the 532 nm laser. (b) The logarithmic photoresponsivity (left) and detectivity (right) as a function of logarithmic optical power at 0.1 V bias voltage. Inset is noise-equivalent power (NEP) as a function of logarithmic optical power at the same condition. (c) Time response characteristic curves of the device at 0.5 V bias voltage. (d) Frequency response characteristic under 532 nm and 1064 nm lasers.

respectively. P, E_e, and A are the input optical power, the laser irradiance, and the effective illumination channel area, respectively. The normalized detectivity D^* in units of Jones ($cm \cdot Hz^{1/2} \cdot W^{-1}$) is given by

$$D^* = \frac{RA^{1/2}}{(2eI_{\text{dark}})^{1/2}}. \tag{2}$$

Here, e is the electron charge. Accordingly, NEP is expressed as

$$\text{NEP} = A^{1/2}/D^*. \tag{3}$$

According to Eqs. (1)–(3), R, D^*, and NEP with various laser powers are plotted in Fig. 2(b). The maximum R of 10^4 $mA \cdot W^{-1}$ was obtained at a low bias of −0.1 V, which showed a significant improvement in magnitude compared with previous studies [24,39]. This improvement arose from two promotional aspects: the 3D GF material and the PTE structure. When compared with single-layer graphene (100 $mA \cdot W^{-1}$) [24], the increase in responsivity by 2 orders of magnitude was attributed to the macro effect of 3D GF, while for the same material (3D GF) [39] the increase arose from the asymmetric electrode design used for the PTE structure.

The relation between R and P can be roughly expressed as $\log R \sim (\beta - 1) \log P$, where β is a parameter without units, and the meaning of β will be discussed later in this article. A good fitting line was achieved, and the value of β was extracted. Additionally, the device showed a high D^* of 10^9 Jones ($cm \cdot Hz^{1/2} \cdot W^{-1}$) and a minimum NEP level of $0.6\ nW \cdot Hz^{-1/2}$.

The response time is another key parameter for a PD and reflects how quickly the optical signal is converted into an electrical signal. The rise and fall times of the photocurrent at 532 nm under 532 mW/cm^2 irradiance and at −0.5 V bias are plotted in Fig. 2(c). According to photocurrent relaxation theory, the carrier lifetimes of the rising and falling edges can be described by using the following equations:

$$I(t) = I_{\text{dark}} + A[\exp(t/\tau_1)] + B[\exp(t/\tau_2)], \tag{4}$$

$$I(t) = I_{\text{dark}} + A[\exp(-t/\tau_1)] + B[\exp(-t/\tau_2)], \tag{5}$$

where I_{dark} is the dark current, τ is the time constant, t is the response time when the laser is switched on and off, and A and B represent scale factors. The rise and fall times were extracted to be 48 ms and 116 ms. This was a much shorter response time compared with a previous report of 26 s [40].

Additionally, a frequency-dependent R is also demonstrated as shown in Fig. 2(d), which was obtained by the frequency-modulated experiment with two lasers with wavelengths of 532 nm and 1064 nm. After normalization to a responsivity at a frequency of 1 Hz, the 3 dB band was determined to be 78 Hz and 84 Hz for the 532 nm and 1064 nm lasers, respectively.

According to the previous expectations on PTE PD and the wide absorption of 3D GF, the response should cover a wide spectral range that includes UV–Vis–NIR–MIR–THz–microwave regions. Then we applied several other wavelengths to the GF PD, which included 405 nm, 808 nm, 10.6 μm (30 THz), 118 μm (2.52 THz), and 1.36 mm (220 GHz). The switched transient photocurrent curves at various wavelengths are presented in the

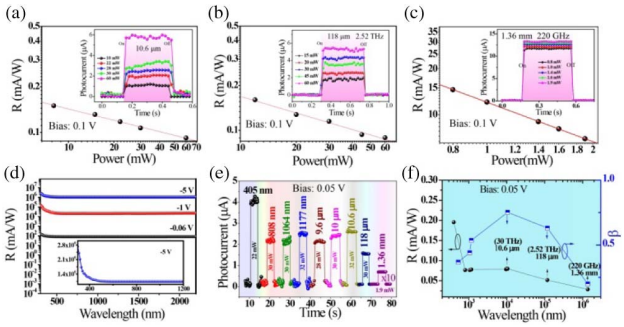

Fig. 3. Double-logarithmic coordinates' photoresponsivities to laser power under (a) 10.6 μm, (b) 118 μm, and (c) 1.36 mm lasers at 0.1 V voltage. Corresponding insets are the switched photocurrent under different irradiances. (d) The broadband photoresponsivity over a wavelength range of 300–2200 nm under different bias voltages (0.06, 1, 5 V). Inset is the applified R within 1200 nm under 5 V voltage. (e) Multiple-wavelength switched photocurrent from 405 nm to 1.36 mm under 0.05 V bias voltage. (f) Full R spectrum (left) and β (right) as a function of wavelength at 0.05 V bias voltage.

insets of Figs. 3(a)–3(c). The saturation photocurrent increased with the increase of the optical power and showed a good switching characteristic with a response time of 40 ms to the 10.6 μm, 118 μm, and 1.36 mm wavelengths. When collecting each saturation photocurrent, R variation with P was obtained and is plotted in double-logarithmic coordinates for the three wavelengths as shown in Figs. 3(a)–3(c). Using the same formula of $\log R \sim (\beta - 1)\log P$, good fitting lines were obtained and values of β could be extracted and shown in Fig. 3(f).

Then we attempted to depict the full spectral response of the GF PD. Figure 3(d) gives the continuous response spectra measured by the grating monochromator and tungsten lamp system under different negative voltages (0.06, 1, and 5 V). Flat and high photoresponsivities were exhibited over a wide range from 300 to 2200 nm, which was consistent with the absorption spectrum. It is worth noting that with the bias increased to 5 V, the photoresponsivity reached a high level of 2.4×10^6 mA · W^{-1} at 300 nm.

Owing to the absence of a measuring system with such a wide range, lasers with various wavelengths were applied to the GF PD at certain specific powers as shown in Fig. 3(e). The applied laser wavelengths ranged from 405 nm to 1.36 mm, and the photocurrent showed steady switching performances. The results strongly confirmed the GF PD could exhibit a response in an ultra-broadband from UV to millimeter wavelengths. The full response spectrum of the GF PD at a very low bias of 0.05 V was eventually obtained and is plotted in Fig. 3(f). A wide, flat, and slowly reduced R with the increase in wavelength is observed. This is completely consistent with the full spectra of the absorption. Based on the linear fitting, each β was also extracted and is plotted in Fig. 3(f). The values first ascended and then descended, and the peak was located at 10.6 μm.

After that we will discuss the mechanism carefully. The schematic diagram of thermoelectric theory can be expressed as Fig. 4(a), setting the x axis along the channel from Au to Ti. When illumination is localized at the center of channel, the

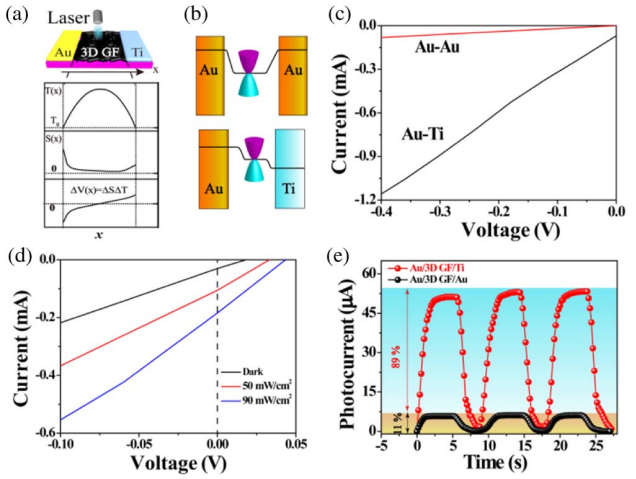

Fig. 4. (a) Photocurrent generation schematic of the 3D GF PD under 532 mm laser illumination. The illumination is localized in the middle of the channel. The x axis forwards from the Au to Ti electrode along the device, and the photopotential generation model over the length of the device including electron temperature $T(x)$, Seebeck coefficient $S(x)$, and potential gradient $\Delta V(x) = \Delta S \Delta T(x)$. (b) Energy band profile of Au/3D GF/Ti and Au/3D GF/Au devices. (c) I–V characteristics of Au/3D GF/Ti and Au/3D GF/Au structures. (d) I–V characteristics of Au/3D GF/Ti under different 532 nm laser illumination intensities. (e) The photocurrent responses of the two different Au/3D GF/Ti and Au/3D GF/Au devices under 532 nm illumination with irradiance of 50 mW · cm^{-2} at 0.01 V bias voltage.

local temperature increases, and around the irradiated region temperature redistributes, as described with $T(x)$ in Fig. 4(a). Then hot carriers generated by thermal excitation locate in a higher temperature region. Subsequently, slow relaxation of the carrier from lattice will occur by thermal decoupling [5,41,42]. Under these conditions, an electrical potential gradient V_{PTE} is created under the hot carriers that flow along the temperature gradient, which is called the PTE effect [42,43]. In principle, under light irradiation due to the different contacts between the 3D GF and the metal electrodes, the local temperature gradients $T(x)$ and the asymmetric Seebeck coefficient $S(x)$ are distributed along the x axis direction within the device. According to the PTE effect, the local temperature gradient $T(x)$ and the Seebeck coefficient $S(x)$ result in a potential gradient $\Delta V(x) = \Delta S \Delta T(x)$ occurring along the axis [5,13,44].

For verification and quantitative analysis of the contributions of the photovoltaic and PTE mechanisms to the photocurrent, we designed a reference device using a symmetrical Au/3D GF/Au electrode structure. Band profile schematics for the two devices are shown in Fig. 4(b). According to Seebeck theory, Au/3D GF/Au shows the symmetric $\Delta S \Delta T(x)$, and then net $\Delta V(x) = 0$. Fig. 4(c) shows the I–V characteristics of the devices with the Au/3D GF/Au and Au/3D GF/Ti electrodes under the same irradiance of 50 mW · cm^{-2} at 532 nm. It displays zero-crossing for symmetric electrode devices, in accordance with PTE theoretical predictions. Moreover, the open circuit voltage of the Au/3D GF/Ti structure (where the Au electrode is positive and the Ti electrode is negative) increases negatively when incident light irradiance rises as shown in Fig. 4(d). This interesting phenomenon indicates that

the photocurrent is dominated by the PTE effect rather than by other effects such as photovoltaic or photoconductive effect. If the photovoltaic mechanisms were valid, a dark I–V curve would almost be zero-crossing. Obviously, it is not the case. For photoconductive effect, we analyzed quantitatively. When devices work at bias, deviating from the zero point, the photoconductive and PTE effects both play a role in the photocurrent. For the symmetric electrode device, the photocurrent comes from the photoconductive mechanism completely; while for the asymmetric electrode device, the photocurrent originates from the PTE effect and photoconductive effect. If the irradiance and bias were the same, the photocurrent from two devices was comparable. The results are shown in Fig. 4(e), where the irradiance of 50 mW · cm^{-2} at the bias −0.01 V. The exact photocurrent value was 52 μA for the asymmetric device and 5.5 μA for the symmetric one, which is almost 1 order of magnitude difference in the saturation photocurrent. In other words, PTE current makes a 90% contribution to the total photocurrent, while the photoconductive current holds 10% in the Au/3D GF/Ti detector. The above analysis gives the first evidence that the PTE effect dominates the photocurrent generation process in our 3D GF device.

The second evidence came from an intuitive MIR image of the *in situ* photoresponse process of the device. According to MIR images and videos, the *in situ* temperature distribution and changes were observed directly. As shown in Fig. 5(a), the insets are the MIR images with and without a 532 nm laser, and the data are extracted from the images. In the dark, the initial temperatures of the electrodes of Au and Ti were 301 K and 299 K, while the 3D GF showed a relatively low temperature of 296 K. When the laser of 532 nm was turned on, the temperature of the irradiated local region immediately and sharply rose by 3.5 K (to 299.5 K). Figure 5(b) shows the temperature (top) and photocurrent (bottom) increments of the device as a function of time. In the process of switching

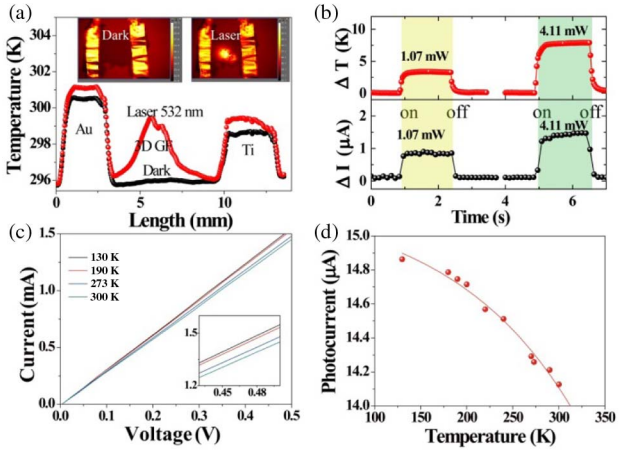

Fig. 5. (a) Temperature distributions of the device at dark and at laser illumination (532 nm, 1 mW). Inset: the MIR image of the device under dark and laser illumination. (b) The temperature (top) and photocurrent (bottom) curves as a function of time at 0.05 V positive bias voltage. (c) I–V characteristics at 532 nm laser of 50 mW/cm^2 illumination under varying temperatures. (d) The photocurrent as a function of temperature from 130 K to 300 K at 50 mW/cm^2 532 nm laser excitation under 0 V bias voltage.

on the light, the trend and the increment of the photocurrent were consistent with that of the temperature. This phenomenon confirmed again that the photocurrent generation was attributed to the PTE effect.

Further confirmation was obtained from the temperature-dependent photocurrent generated by 532 nm laser. According to PTE, the current (I) is proportional to $(S_2 - S_1)/\kappa$, where κ is the thermal conductivity [45]. Given S is approximately linear to T, and κ has an exponential dependence on T, then the relationship $I \sim T^{1-\alpha}$ can be deduced, where $\alpha > 1$. Based on the varying temperature I–V curves [shown in Fig. 5(c)], some current points at a specific bias with various temperatures were collected and are plotted in Fig. 5(d). A good fitting was performed on the I–V curve by using the relation $I \sim 1/T^{\alpha-1}$, and then α was obtained from fitting the data as $\alpha = 2.2$. Therefore, the requirement of $\alpha > 1$ was met and was in good agreement with the out-of-plane acoustic phonon mode based on thermal conductivity theory [17]. It confirmed the PTE effect thirdly.

Finally, we wish to discuss the meaning of β. Based on the PTE effect, the photocurrent can be expressed as

$$\Delta I = \Delta V/R' = \Delta S \cdot \Delta T/\kappa, \tag{6}$$

where ΔS is the difference of the Seebeck coefficient and ΔT is the change of temperature caused by light. Setting ΔT to have a power law dependence on P^β, where P is the incident laser power, then, the responsivity R is proportional to $P^{\beta-1}/T^{\alpha-1}$. After the logarithmic function, $\log R \propto (\beta - 1)\log P - (\alpha - 1)\log T$ is obtained.

Therefore, according to the above fittings in Fig. 2(b) and Figs. 3(a)–3(c), the term for absolute temperature (T) can be viewed as a constant, and the first optical power term plays a major role in the responsivity. The meaning of β can be interpreted as the degree of temperature increase caused by light. According to Fig. 3(f), when a 10.6 μm laser was incident on the detector, β reached the maximum. This demonstrates that light with a wavelength of 10.6 μm has the highest photothermoelectric conversion degree.

4. CONCLUSION

In summary, we have successfully fabricated an ultra-broadband, highly photosensitive 3D GF PD. Impressive performances have been obtained at room temperature, including a non-wavelength selective photoresponse, a highest photoresponsivity of 10^3 A · W^{-1}, a short response time of 48 ms, and a 3 dB band of 80 Hz. Notably, a flat and ultra-broadband spectral response is observed over the range from 300 nm to 1.36 mm (220 GHz), which covers 4 orders of magnitude in wavelength. Three sources of evidence point to the PTE mechanism. Furthermore, the wavelength-dependent β is given and is interpreted as the photothermoelectric conversion degree. Our work paves a way to realize uncooled, ultra-broadband, and highly sensitive 3D GF PDs with full spectral continuity from ultraviolet to the microwave regions, which has a wide application area in THz detection, imaging, night vision systems, and remote sensing.

Funding. National Natural Science Foundation of China (61675147, 61605141, 61735010, 91838301); National Key Research and Development Program of China (2017YFA0700202); Basic Research Program of Shenzhen (JCYJ20170412154447469); Beiyang Yong Junior Faculties of Tianjin University (2019XRG-0056); Wenzhou City Governmental Public Industrial Technology Project (G20160014).

Disclosures. The authors declare no conflicts of interest.

REFERENCES

1. T. Deng, Z. Zhang, Y. Liu, Y. Wang, F. Su, S. Li, Y. Zhang, H. Li, H. Chen, Z. Zhao, Y. Li, and Z. Liu, "Three-dimensional graphene field-effect transistors as high-performance photodetectors," Nano Lett. **19**, 1494–1503 (2019).
2. Y. Liu, J. Yin, P. Wang, Q. Hu, Y. Wang, Y. Xie, Z. Zhao, Z. Dong, J. L. Zhu, W. Chu, N. Yang, J. Wei, W. Ma, and J. L. Sun, "High-performance, ultra-broadband, ultraviolet to terahertz photodetectors based on suspended carbon nanotube films," ACS Appl. Mater. Interf. **10**, 36304–36311 (2018).
3. H. Fang and W. Hu, "Photogating in low dimensional photodetectors," Adv. Sci. **4**, 1700323 (2017).
4. N. Guo, W. Hu, T. Jiang, F. Gong, W. Luo, W. Qiu, P. Wang, L. Liu, S. Wu, L. Liao, X. Chen, and W. Lu, "High-quality infrared imaging with graphene photodetectors at room temperature," Nanoscale **8**, 16065–16072 (2016).
5. F. H. Koppens, T. Mueller, P. Avouris, A. C. Ferrari, M. S. Vitiello, and M. Polini, "Photodetectors based on graphene, other two-dimensional materials and hybrid systems," Nat. Nanotechnol. **9**, 780–793 (2014).
6. J. Li, L. Niu, Z. Zheng, and F. Yan, "Photosensitive graphene transistors," Adv. Mater. **26**, 5239–5273 (2014).
7. Z. Liu, S. P. Lau, and F. Yan, "Functionalized graphene and other two-dimensional materials for photovoltaic devices: device design and processing," Chem. Soc. Rev. **44**, 5638–5679 (2015).
8. Z. Sun, Z. Liu, J. Li, G.-A. Tai, S.-P. Lau, and F. Yan, "Infrared photodetectors based on CVD-grown graphene and PbS quantum dots with ultrahigh responsivity," Adv. Mater. **24**, 5878–5883 (2012).
9. V. Adinolfi and E. H. Sargent, "Photovoltage field-effect transistors," Nature **542**, 324–327 (2017).
10. M. Tonouchi, "Cutting-edge terahertz technology," Nat. Photonics **1**, 97–105 (2007).
11. R. CiupaAntoni and R. Rogalski, "Performance limitations of photon and thermal infrared detectors," Opto-Electron. Rev. **5**, 257–266 (1997).
12. F. H. L. Koppens, T. Mueller, P. Avouris, A. C. Ferrari, M. S. Vitiello, and M. Polini, "Photodetectors based on graphene, other two-dimensional materials and hybrid systems," Nat. Nanotechnol. **9**, 780–793 (2014).
13. V. Shautsova, T. Sidiropoulos, X. Xiao, N. A. Gusken, N. C. G. Black, A. M. Gilbertson, V. Giannini, S. A. Maier, L. F. Cohen, and R. F. Oulton, "Plasmon induced thermoelectric effect in graphene," Nat. Commun. **9**, 5190 (2018).
14. W. Liu, W. Wang, Z. Guan, and H. Xu, "A plasmon modulated photo-thermoelectric photodetector in silicon nanostripes," Nanoscale **11**, 4918–4924 (2019).
15. S. Limpert, A. Burke, I. J. A. Chen, N. Anttu, S. Lehmann, S. Fahlvik, S. Bremner, G. Conibeer, C. Thelander, M. E. Pistol, and H. Linke, "Bipolar photothermoelectric effect across energy filters in single nanowires," Nano Lett. **17**, 4055–4060 (2017).
16. X. Cai, A. B. Sushkov, R. J. Suess, M. M. Jadidi, G. S. Jenkins, L. O. Nyakiti, R. L. Myers-Ward, S. Li, J. Yan, D. K. Gaskill, T. E. Murphy, H. D. Drew, and M. S. Fuhrer, "Sensitive room-temperature terahertz detection via the photothermoelectric effect in graphene," Nat. Nanotechnol. **9**, 814–819 (2014).
17. X. Xu, N. M. Gabor, J. S. Alden, A. M. van der Zande, and P. L. McEuen, "Photo-thermoelectric effect at a graphene interface junction," Nano Lett. **10**, 562–566 (2010).
18. M. He, Y. J. Lin, C. M. Chiu, W. Yang, B. Zhang, D. Yun, Y. Xie, and Z.-H. Lin, "A flexible photo-thermoelectric nanogenerator based on MoS_2 PU photothermal layer for infrared light harvesting," Nano Energy **49**, 588–595 (2018).
19. N. M. Jia Qi, X. Ma, R. Adelung, and Y. Yang, "Enhanced photocurrent in $BiFeO_3$ materials by coupling temperature and thermo-phototronic effects for self-powered ultraviolet photodetector system," ACS Appl. Mater. Interface **10**, 13712–13719 (2018).
20. M. Zhao, D. Kim, V. L. Nguyen, J. Jiang, L. Sun, Y. H. Lee, and H. Yang, "Coherent thermoelectric power from graphene quantum dots," Nano Lett. **19**, 61–68 (2019).
21. Z. Zheng, J. Yao, L. Zhu, W. Jiang, B. Wang, G. Yang, and J. Li, "Tin dioxide quantum dots coupled with graphene for high-performance bulk-silicon Schottky photodetector," Mater. Horizons **5**, 727–737 (2018).
22. D. Paria, H. H. Jeong, V. Vadakkumbatt, P. Deshpande, P. Fischer, A. Ghosh, and A. Ghosh, "Graphene-silver hybrid devices for sensitive photodetection in the ultraviolet," Nanoscale **10**, 7685–7693 (2018).
23. Y. Zhu, S. Murali, W. Cai, X. Li, J. W. Suk, J. R. Potts, and R. S. Ruoff, "Graphene and graphene oxide: synthesis, properties, and applications," Adv. Mater. **22**, 3906–3924 (2010).
24. A. V. Emelianov, D. Kireev, A. Offenhäusser, N. Otero, P. M. Romero, and I. I. Bobrinetskiy, "Thermoelectrically driven photocurrent generation in femtosecond laser patterned graphene junctions," ACS Photon. **5**, 3107–3115 (2018).
25. X. Wang, Z. Cheng, K. Xu, H. K. Tsang, and J.-B. Xu, "High-responsivity graphene/silicon-heterostructure waveguide photodetectors," Nat. Photonics **7**, 888–891 (2013).
26. H. Chang and H. Wu, "Graphene-based nanomaterials: synthesis, properties, and optical and optoelectronic applications," Adv. Funct. Mater. **23**, 1984–1997 (2013).
27. G. J. Amador, Z. Ren, A. F. Tabak, Y. Alapan, O. Yasa, and M. Sitti, "Temperature gradients drive bulk flow within microchannel lined by fluid-fluid interfaces," Small **15**, 1900472 (2019).
28. G. Li, L. Liu, G. Wu, W. Chen, S. Qin, Y. Wang, and T. Zhang, "Self-powered UV-near infrared photodetector based on reduced graphene oxide/n-Si vertical heterojunction," Small **12**, 5019–5026 (2016).
29. W. Chen, P. Xiao, H. Chen, H. Zhang, Q. Zhang, and Y. Chen, "Polymeric graphene bulk materials with a 3D cross-linked monolithic graphene network," Adv. Mater. **31**, 1802403 (2018).
30. K. Zhao, T. Zhang, H. Chang, Y. Yang, P. Xiao, H. Zhang, C. Li, C. Sekhar Tiwary, P. M. Ajayan, and Y. Chen, "Super-elasticity of three-dimensionally cross-linked graphene materials all the way to deep cryogenic temperatures," Sci. Adv. **5**, eaav2589 (2019).
31. Y. Zhang, Y. Huang, T. Zhang, H. Chang, P. Xiao, H. Chen, Z. Huang, and Y. Chen, "Broadband and tunable high-performance microwave absorption of an ultralight and highly compressible graphene foam," Adv. Mater. **27**, 2049–2053 (2015).
32. Y. Yang, R. Zhao, T. Zhang, K. Zhao, P. Xiao, Y. Ma, P. M. Ajayan, G. Shi, and Y. Chen, "Graphene-based standalone solar energy converter for water desalination and purification," ACS Nano **12**, 829–835 (2018).
33. L. T. Duy, D.-J. Kim, T. Q. Trung, V. Q. Dang, B.-Y. Kim, H. K. Moon, and N.-E. Lee, "High performance three-dimensional chemical sensor platform using reduced graphene oxide formed on high aspect-ratio micro-pillars," Adv. Funct. Mater. **25**, 883–890 (2015).
34. P. R. Golam Haider, C.-W. Chiang, W.-C. Tan, Y.-R. Liou, H.-T. Chang, C.-T. Liang, W.-H. Shih, and Y.-F. Chen, "Electrical-polarization-induced ultrahigh responsivity photodetectors based on graphene and graphene quantum dots," Adv. Funct. Mater. **26**, 620–628 (2016).
35. Y. Ma and Y. Chen, "Three-dimensional graphene networks: synthesis, properties and applications," Nat. Sci. Rev. **2**, 40–53 (2015).
36. H. C. Zhiyu Huang, Y. Huang, Z. Ge, Y. Zhou, Y. Yang, P. Xiao, J. Liang, T. Zhang, Q. Shi, G. Li, and Y. Chen, "Ultra-broadband wide-angle terahertz absorption properties of 3D graphene foam," Adv. Funct. Mater. **28**, 1704363 (2017).
37. Y. Liu, F. Wang, X. Wang, X. Wang, E. Flahaut, X. Liu, Y. Li, X. Wang, Y. Xu, Y. Shi, and R. Zhang, "Planar carbon nanotube-graphene hybrid films for high-performance broadband photodetectors," Nat. Commun. **6**, 98589 (2015).

38. Y. Yu, Y. Zhang, Z. Zhang, H. Zhang, X. Song, M. Cao, Y. Che, H. Dai, J. Yang, J. Wang, H. Zhang, and J. Yao, "Broadband phototransistor based on $CH_3NH_3PbI_3$ perovskite and PbSe quantum dot heterojunction," J. Phys. Chem. Lett. **8**, 445–451 (2017).
39. Y. C. Hua Tian, J. Sunc, and J. He, "Enhanced broadband photoresponse of substrate-free reduced graphene oxide photodetectors," RSC Adv. **7**, 46536–46544 (2017).
40. B. Chitara, L. S. Panchakarla, S. B. Krupanidhi, and C. N. Rao, "Infrared photodetectors based on reduced graphene oxide and graphene nanoribbons," Adv. Mater. **23**, 5419–5424 (2011).
41. M. W. Graham, S.-F. Shi, D. C. Ralph, J. Park, and P. L. McEuen, "Photocurrent measurements of supercollision cooling in graphene," Nat. Phys. **9**, 103–108 (2012).
42. J. C. Song, M. S. Rudner, C. M. Marcus, and L. S. Levitov, "Hot carrier transport and photocurrent response in graphene," Nano Lett. **11**, 4688–4692 (2011).
43. D. Sun, G. Aivazian, A. M. Jones, J. S. Ross, W. Yao, D. Cobden, and X. Xu, "Ultrafast hot-carrier-dominated photocurrent in graphene," Nat. Nanotechnol. **7**, 114–118 (2012).
44. Q. Wang, C. Z. Li, S. Ge, J. G. Li, W. Lu, J. Lai, X. Liu, J. Ma, D. P. Yu, Z. M. Liao, and D. Sun, "Ultrafast broadband photodetectors based on three-dimensional dirac semimetal Cd_3As_2," Nano Lett. **17**, 834–841 (2017).
45. X. Xu, N. M. Gabor, J. S. Alden, A. M. van der Zande, and P. L. McEuen, "Photo-thermoelectric effect at a graphene interface junction," Nano Lett. **10**, 562–566 (2010).